RAA 2019 Vol. **19** No. **10**, 151(17pp) doi: 10.1088/1674–4527/19/10/151

http://www.raa-journal.org *http://iopscience.iop.org/raa*

Research in Astronomy and Astrophysics

GABE: Galaxy Assembly with Binary Evolution

Zhen Jiang[1,2], Jie Wang[1,2], Liang Gao[1,2,3], Feng-Hui Zhang[4,5], Qi Guo[1,2], Lan Wang[1] and Jun Pan[1]

[1] Key Laboratory for Computational Astrophysics, National Astronomical Observatories, Chinese Academy of Sciences, Beijing 100101, China; *zjiang@nao.cas.cn, jie.wang@nao.cas.cn*
[2] School of Astronomy and Space Science, University of Chinese Academy of Sciences, Beijing 100049, China
[3] Institute of Computational Cosmology, Department of Physics, University of Durham, South Road, Durham DH1 3LE, UK
[4] Yunnan Observatories, Chinese Academy of Sciences, Kunming 650011, China
[5] Key Laboratory for the Structure and Evolution of Celestial Objects, Chinese Academy of Sciences, Kunming 650011, China

Received 2019 March 15; accepted 2019 May 15

Abstract We developed a new semi-analytic galaxy formation model: Galaxy Assembly with Binary Evolution (GABE). For the first time, we introduce binary evolution into semi-analytic models of galaxy formation by using the Yunnan-II stellar population synthesis model, which includes various binary interactions. When implementing our galaxy formation model onto the merger trees extracted from the Millennium simulation, it can reproduce a large body of observational results. We find that in the local universe, the model including binary evolution reduces the luminosity at optical and infrared wavelengths slightly, but it increases the luminosity at ultraviolet wavelengths significantly, especially in $F_{\rm UV}$ band. The resulting luminosity function does not change very much over SDSS optical bands and infrared band, but the predicted colors are bluer, especially when the $F_{\rm UV}$ band is under consideration. The new model allows us to explore the physics of various high energy events related to the remnants of binary stars, such as type Ia supernovae, short gamma-ray bursts and gravitational wave events, and their relation with host galaxies in a cosmological context.

Key words: galaxies: formation — galaxies: luminosity function, mass function — galaxies: stellar content

1 INTRODUCTION

In the framework of ΛCDM cosmology, semi-analytic models of galaxy formation effectively simulate the formation and evolution of galaxies, and have played an indispensable role during the building of the current galaxy formation theory from the early-1990s to 2010s (White & Frenk 1991; Kauffmann et al. 1999; Springel et al. 2001; Croton et al. 2006; De Lucia & Blaizot 2007; Guo et al. 2011; Henriques et al. 2015). This method is very successful when used to explore the effect of various physical processes on galaxy formation. However, some physical models still need further investigation, including binary evolution.

It is well-known that more than ∼50% of field stars and ∼70% of stars in massive young star clusters are in binary systems, with only a relatively small fraction of stars being single (e.g., Duquennoy & Mayor 1991; Sana et al. 2012). Binary stars undergo many different physical processes from single stars, such as mass transfer, mass accretion, common envelope (CE) evolution, collisions, supernova kicks, tidal evolution and angular momentum loss. Such binary interactions change the color and spectral energy distribution (SED) of the entire stellar population (Pols & Marinus 1994; Han et al. 2002). Though binary evolution could influence photometric properties of stellar populations, which will certainly further influence the properties of galaxies, most existing semi-analytic models adopt classical single stellar population synthesis models (SPSMs), such as BC03 (Bruzual & Charlot 2003), CB07 (Bruzual 2007) and M05 (Maraston 2005).

Another motivation to use the SPSM with binary evolution is that many high energy astrophysical events are consequences of binary evolution. For example, short gamma-ray bursts are thought to be products of double neutron star (NS-NS) or neutron star-black hole (NS-BH) mergers (Narayan et al. 1992); supernova Ia events are due

to white dwarf and non-degenerate companion evolution (Whelan & Iben 1973) or double white dwarf (WD-WD) mergers (Iben & Tutukov 1984); and gravitational wave events are supposed to be triggered by the merger of two compact objects in binary systems. Furthermore, fast radio burst events are possibly connected with binary NS mergers (Totani 2013; Wang et al. 2016). With the rapid increase in the number of detections of such high energy events at a wide range of redshift, a large sample of such events may be investigated in a cosmological context in the near future. Therefore, it is timely to adopt an SPSM with binary evolution in a galaxy formation model to explore the connection between such events, and their relationship with their host galaxies, over the history of the Universe.

In this paper, we have developed a new semi-analytic model Galaxy Assembly with Binary Evolution (GABE). The model incorporates many physical recipes from existing successful semi-analytic models and includes some new ingredients, for example, adopting an SPSM with binary evolution–Yunnan-II model and a cooling table of Wiersma09 (Wiersma et al. 2009) which treats the effect of photoionization on gas cooling quite carefully. In GABE, we explicitly track the evolution of binary systems in each simple stellar population[1] produced in the formation of each galaxy in the cosmic background. By recording the evolution of each binary event, especially its final fate as a remnant of merging binaries, which are supposed to be associated with the high energy events mentioned above, our model is able to predict every such high energy event in each galaxy across cosmic time.

The structure of this paper is as follows. In Section 2, we introduce the N-body simulation that we apply in this work and we describe our galaxy formation model in detail. The results of our semi-analytic models are demonstrated in Section 3. Finally, we summarize our results in Section 4.

2 GALAXY FORMATION MODELS

In this section, we describe the N-body simulation and all of the physical models used in GABE. The physical driving models for galaxy formation have been developing gradually in the past decades (White & Frenk 1991; Kauffmann et al. 1999; Springel et al. 2001; Croton et al. 2006; De Lucia & Blaizot 2007; Guo et al. 2011; Henriques et al. 2015). In our model, we follow these successes and consider a full set of known physical models for galaxy formation. Apart from these semi-analytic models, cosmological hydrodynamic simulation is another method of modeling the formation and evolution of galaxies. Hydrodynamic simulations have the advantage of being able to reproduce the physical processes in more detail than the semi-analytic method, while the latter requires less computational cost and is therefore more flexible in tuning and testing model parameters. Cosmological hydrodynamic simulations have achieved huge successes in recovering galaxies' statistical properties in recent years (e.g., Schaye et al. 2015; Nelson et al. 2018), and there are some works which have successfully planted binary evolution into existing hydrodynamic simulations by post-processes (e.g., Mapelli et al. 2017). However, there is as yet no binary evolution in semi-analytic models. In this work, by combining binary SPSMs with semi-analytic models, the calculation of binary properties of galaxies can be done on-the-fly and will not be limited by the time resolution of snapshots, which is more suitable for generating a mock galaxy catalog with binaries or double compact objects (DCOs) for larger volume.

In Section 2.1, the N-body simulation utilized in GABE is introduced. The other subsections describe in detail our galactic formation models. Note that most of the physical models described in this work are the same as in Guo et al. (2011), which is a well-accepted semi-analytic model. Compared with Guo et al. (2011), our modifications focus on hot gas cooling (Sect. 2.2.2) and SPSMs (Sect. 2.4.1). In Section 2.2, we describe all physical processes involved in the evolution of an *isolated* galaxy, including reionization, gas cooling, star formation, supernova feedback, BH growth, active galactic nucleus (AGN) feedback and bar formation. A subsection on exchanges of mass, metals and angular momentum follows as a short summary. We then describe how to treat galaxy mergers in our model in Section 2.3, and how to calculate galaxies' luminosity in Section 2.4. Finally, we discuss our model calibration in Section 2.5.

2.1 N-body Simulation

In this study, we take advantage of dark matter merger trees from the Millennium-I Simulation (Springel et al. 2005), which is widely employed for studies of galaxy formation and evolution because of its good combination of large box size and relatively high mass resolution. Its box size is $L_{\rm box} = 685\,{\rm Mpc}$ and mass of simulation particle is $1.18 \times 10^9\,M_\odot$. Accordingly, its halo resolution is $2.36 \times 10^{10}\,M_\odot$, which is 20 times the particle mass. These features ensure the following semi-analytic models can generate a complete galaxy catalog for galaxies more massive than $\sim 10^8\,M_\odot$ and suppress cosmic variances at the same time. The Millennium-I simulation assumes a WMAP1 cosmology with $\Omega_{\rm m} = 0.25$, $\Omega_{\rm b} = 0.045$, $\Omega_\Lambda =$

[1] A simple stellar population represents a set of stars which have the same age and metallicity. "Simple" is used to distinguish it from a so-called complex stellar population, which is composed of multiple simple stellar populations.

0.75, $n = 1$, $\sigma_8 = 0.9$ and $H_0 = 73\,\mathrm{km\,s^{-1}\,Mpc^{-1}}$, which are derived from a combined analysis of the 2dFGRS (Colless & et al. 2001) and the first-year WMAP data (Spergel et al. 2003). The merger trees are built based on the D-halo catalog (Jiang et al. 2014).

2.2 Evolution of Isolated Galaxies

2.2.1 Cosmic reionization

It is now well accepted that photoheating by ultraviolet (UV) background significantly lowers gas content in dwarf sized dark matter halos. Here we use a formula put forward by Gnedin (2000)

$$f_b(M,z) = f_b^c \left[1 + \left(2^{\alpha/3} - 1\right)\left(\frac{M}{M_c(z)}\right)^{-\alpha}\right]^{-\frac{3}{\alpha}}, \quad (1)$$

where f_b^c is mean cosmic baryon fraction, which is 17% in WMAP1 cosmology, and M is the total halo mass, including dark matter and baryons. There are two parameters in Equation (1): α and $M_c(z)$. With larger α, the baryonic fraction decreases more rapidly with decreasing halo mass. $M_c(z)$ is the characteristic mass below which halos only contain less than 50 percent of universal baryon fraction. Here we adopt the latest results from Okamoto et al. (2008): $\alpha = 2$; $M_c \approx 10^7\,h^{-1}\,M_\odot$ just after reionization and $M_c \approx 6.49 \times 10^9\,h^{-1}\,M_\odot$ at $z = 0$, as depicted in figure 3 of Okamoto et al. (2008).

2.2.2 Gas cooling with background radiation

When gas falls into the potential well of a dark matter halo, it will be shock-heated. This hot and dense gas will then cool down by radiating away the energy. If the cooling rate of the gas is fast enough, gas can cool and condense to the center of the halo at the free-fall rate. Otherwise, a shock-front will form and heat the gas to about the virial temperature of the halo. Because the gas has to cool down before it can settle down to the central galaxy through cooling flows, the cooling rate of gas determines the amount of gas that can settle to the center.

The local cooling timescale of the gas is usually estimated as

$$t_{\rm cool}(r) = \frac{T}{{\rm d}T/{\rm d}t} = \frac{\frac{3}{2}n(r)kT}{\mathcal{L}(r)}, \quad (2)$$

where $n(r)$ is the number density of the gas at radius r, and can be estimated by $n(r) = \rho(r)/\mu m_{\rm p}$; $\rho(r)$ is the local density of the hot gas, which is assumed to be an isothermal profile in our model: $\rho(r) \propto r^{-2}$; μ is the mean molecular mass, and $m_{\rm p}$ is the proton mass; k is the Boltzmann constant; T is the temperature of gas; $\mathcal{L}$ is the cooling rate per unit volume of gas with a unit of $\mathrm{erg\,s^{-1}\,cm^{-3}}$.

"Cooling radius," $R_{\rm cool}$, is quite commonly used in many semi-analytic models. For a given dark matter halo, we follow Springel et al. (2001) to define cooling radius as the radius within which the gas can cool in a dynamical timescale, i.e., $t_{\rm cool}(R_{\rm cool}) = t_{\rm dyn,h}$, and

$$t_{\rm dyn,h} = \frac{R_{\rm vir}}{V_{\rm vir}} = 0.1H(z)^{-1}. \quad (3)$$

If $R_{\rm cool} > R_{\rm vir}$, the halo is in the rapid infall regime. Gas condenses to the halo center at the rate of free fall

$$\dot{M}_{\rm cool} = \frac{M_{\rm hot}}{t_{\rm dyn,h}}. \quad (4)$$

If $R_{\rm cool} < R_{\rm vir}$, then the shock front forms at $R_{\rm cool}$ and only the gas inside $R_{\rm cool}$ can condense to the center. Because the hot gas profile in a halo is assumed to be isothermal, we have

$$\dot{M}_{\rm cool} = \frac{M_{\rm hot}}{t_{\rm dyn,h}}\frac{R_{\rm cool}}{R_{\rm vir}}. \quad (5)$$

The cooling rate $\mathcal{L}$ adopted in many existing semi-analytic galaxy formation models assumes the collisional ionization equilibrium (CIE) assumption, which means the ions and electrons in the gas are in collisional equilibrium, and background radiation is ignored. With the CIE assumption, the cooling rate of low density plasma is simply proportional to the gas density squared: $\mathcal{L} = n^2\Lambda(T_{\rm hot}, Z_{\rm hot})$. Λ is the so-called "cooling function" and has the unit of $\mathrm{erg\,s^{-1}\,cm^3}$. Λ only depends on the temperature and metallicity of the gas and can be conveniently calculated and tabulated (e.g., Sutherland & Dopita 1993). However, generally circumgalacitc medium (CGM) is not in the CIE state. Efstathiou (1992) found that a significant UV background radiation is already in place while galaxies form and can lengthen the cooling timescale of gas. Wiersma et al. (2009) (hereafter Wiersma09[2]) provided a cooling table by quite carefully taking UV background radiation into account. We adopt this table in our model.

When considering UV radiation background, the cooling rate $\mathcal{L}$ is no longer simply proportional to gas density squared. However, we can still use density squared to normalize the table for easier usage. In Wiersma09, the relation is $\mathcal{L} = n_{\rm H}^2\Lambda(T, Z, n_{\rm He}/n_{\rm H}, n_{\rm H}, z)$, where T and Z are the temperature and metallicity of gas, respectively, $n_{\rm H}$ and $n_{\rm He}$ are the number densities of hydrogen and helium, respectively, and z is the redshift.

The cooling table of Wiersma09 cannot be easily applied because of two reasons: (1) The cooling function depends on local density $n_{\rm H}$ which varies with radius. Therefore the equation $t_{\rm cool}(r) = t_{\rm dyn,h}$ can only be solved numerically. (2) We use equation (5) in Wiersma

[2] The cooling tables are offered on their website: `http://www.strw.leidenuniv.nl/WSS08/`.

et al. (2009) to calculate the cooling function, therefore we have to look up eight tables to get one cooling rate. This is extremely time consuming. To overcome these problems, we simplify the calculation as described in the following two steps:

(1) We decrease the radius dependence by assuming the gas has a uniform temperature, metallicity and composition distribution along radius, i.e. we estimate gas temperature as the virial temperature of the host dark matter halo, $T = T_{\rm vir} = \frac{1}{2}\frac{\mu m_{\rm H}}{k} V_{\rm vir}^2 = 35.9 (V_{\rm vir}/\ {\rm km\ s^{-1}})^2\,{\rm K}$, and estimate the mean molecular mass and composition of gas as the fully ionized primordial gas, $\mu = 0.59$ and $n_{\rm He}/n_{\rm H} = 0.083$.

(2) With these assumptions, the left side of the equation $t_{\rm cool} = t_{\rm dyn,h}$ is a function of $(T, Z, n_{\rm H}, z)$, and its right side is a function of redshift z (as $t_{\rm dyn,h} = 0.1 H(z)^{-1}$). We can see that this relation is not halo dependent, which means that we can solve this equation before running the semi-analytic model and save a lot of CPU time. Thus, we re-assemble tables of Wiersma et al. (2009) to a new one, $n_{\rm H,crit}(T, Z, z)$. Here $n_{\rm H,crit}$ is the gas density where $t_{\rm cool}(n_{\rm H,crit}) = t_{\rm dyn,h}$. To determine $n_{\rm H,crit}$, we calculate $t_{\rm cool}$ at each density bin of Wiersma et al. (2009), from high density to low density, compare $t_{\rm cool}$ with $t_{\rm dyn,h}$, then record the first highest density when $t_{\rm cool} \geq t_{\rm dyn,h}$ as $n_{\rm H,crit}$. This table is pre-made and suitable for different situations in the models.

Therefore we only need to look up this table one time to get the $n_{\rm H,crit}$, and we can easily transfer the critical density into cooling radius by

$$R_{\rm cool} = \left[\frac{X M_{\rm hot}}{4\pi m_{\rm p} R_{\rm vir} n_{\rm H,crit}(T_{\rm hot}, Z_{\rm hot}, z)}\right]^{\frac{1}{2}}, \quad (6)$$

where $X = 0.75$ is the mass fraction of hydrogen in primordial gas.

2.2.3 Star formation

As gas condenses to the center of a dark matter halo, it will form a rotation supported cold gas disk because of angular momentum conservation. If the local density of gas exceeds a critical value, then stars will eventually form. The critical surface density at radius r is suggested by Kauffmann (1996)

$$\Sigma_{\rm crit}(r) = 12 \left(\frac{V_{\rm max}}{200\ {\rm km\ s^{-1}}}\right) \left(\frac{r}{10\,{\rm kpc}}\right)^{-1} M_\odot {\rm pc}^{-2}, \quad (7)$$

where $V_{\rm max}$ is the maximum circular velocity of the dark matter halo. Integrating $\Sigma_{\rm crit}(r)$ from 0 to three times scale radius of the gaseous disk, as suggested by Croton et al. (2006), the critical gas disk mass reads

$$M_{\rm crit} = 11.5 \times 10^9 \left(\frac{V_{\rm max}}{200\ {\rm km\ s^{-1}}}\right) \left(\frac{R_{\rm disk,gas,d}}{10\,{\rm kpc}}\right) M_\odot, \quad (8)$$

where $R_{\rm disk,gas,d}$ is the exponential scale radius of the cold gas disk. Therefore for disks with $M_{\rm disk,gas} > M_{\rm crit}$, a certain amount of the gas will be converted into stars

$$\dot{M}_{\rm SF,disk} = \alpha \left(M_{\rm disk,gas} - M_{\rm crit}\right)/t_{\rm dyn}, \quad (9)$$

where $t_{\rm dyn} = 3R_{\rm disk,gas,d}/V_{\rm max}$ is the characteristic timescale at the edge of the star-forming disk and α is the "star formation efficiency," which is a free parameter. Here, a fiducial value of 0.02 is adopted.

For cold gas in a spheroid, we use a star-formation timescale scheme from Benson (2011) to calculate its star formation rate

$$\dot{M}_{\rm SF,sph} = M_{\rm sph,gas}/t_{\rm sf,sph}, \quad (10)$$

$$\begin{aligned} t_{\rm sf,sph} &= 10 \left(\frac{V_{\rm sph}}{200\ {\rm km\ s^{-1}}}\right)^{-1.5} t_{\rm dyn} \\ &= 10 \left(\frac{V_{\rm sph}}{200\ {\rm km\ s^{-1}}}\right)^{-1.5} \left(\frac{R_{\rm sph,gas}}{V_{\rm sph}}\right), \end{aligned} \quad (11)$$

where $t_{\rm sf,sph}$ is the star-formation timescale in the spheroidal component, $V_{\rm sph}$ is the characteristic velocity of the spheroid and $R_{\rm sph,gas}$ is the half mass radius of the gas in the spheroid.

2.2.4 Supernova feedback

Once stars form, they are assumed to follow the evolutionary tracks of the standard stellar evolution model, become increasingly metal rich, and eventually release a large amount of mass and energy into their surroundings. We adopt the instantaneous stellar evolution assumption, which assumes that stars evolve to their final states (e.g., $t_{\rm age} \sim 10\,{\rm Gyr}$) right after their birth. Compared to the relatively large timesteps that are implemented in semi-analytic models, such a simplification is acceptable. A non-instantaneous scheme is also explored by other authors, such as De Lucia et al. (2014). During this instantaneous evolution, we assume 43% of stellar mass is recycled back to the CGM, and the mass of created metals is 3% of the initial stellar mass, which is in agreement with the Chabrier (2003) initial mass function (IMF) that we use.

As stars evolve into their final state, they may instantaneously release a large amount of energy into the interstellar medium (ISM) through supernova explosion. During this process, the ISM temperature may increase and suppress further star formation. If the ejected energy is large enough, some gas may be ejected out of the galaxy. In our

model, the energy of the supernova is first used to reheat cold gas back to the hot gas phase. If the temperature of the reheated hot gas is higher than the virial temperature of the dark matter halo, the excess energy will be used to put gas into an ejecta component, called "outflow," which will not be able to cool back within a certain timescale.

The amount of reheated cold gas is estimated as

$$\delta M_{\rm reheat} = \epsilon_{\rm reheat} \times \delta M_{\rm SF}, \tag{12}$$

$$\epsilon_{\rm reheat} = \epsilon \times \left[0.5 + \left(\frac{V_{\rm max}}{V_{\rm max,c}}\right)^{-\beta_1}\right], \tag{13}$$

where ϵ and β_1 are free parameters describing the heating efficiency of newly formed stars, and $V_{\rm max,c}$ is a characteristic velocity used to adjust the shape of $\epsilon_{\rm reheat}$. We also make sure that the energy of reheated gas will not be larger than the energy of the supernova

$$\delta E_{\rm reheat} = \frac{1}{2}\delta M_{\rm reheat} V_{\rm vir}^2 \leq \delta E_{\rm SN} = \frac{1}{2}\delta M_{\rm SF} V_{\rm SN}^2, \tag{14}$$

where $\delta E_{\rm reheat}$ is energy of the reheated gas, $\delta E_{\rm SN}$ is the available supernova energy, $V_{\rm SN} = 630$ km s^{-1} is the characteristic wind speed of the supernova. If $\delta E_{\rm SN} > \delta E_{\rm reheat}$, then we use a certain amount of excess energy to heat more hot gas to virial temperature and include it in an ejecta component

$$\delta M_{\rm eject} = \frac{\epsilon_{\rm eject}\delta E_{\rm SN} - \delta E_{\rm reheat}}{\frac{1}{2}V_{\rm vir}^2}, \tag{15}$$

where

$$\epsilon_{\rm eject} = \eta \times \left[0.5 + \left(\frac{V_{\rm max}}{V_{\rm max,c}}\right)^{-\beta_2}\right] \tag{16}$$

describes the ejection efficiency. We require $\epsilon_{\rm eject} \leq 1$. Here, η, β_2 and $V_{\rm max,c}$ are free parameters.

The ejected gas may return to the hot gas halo due to gravitational attraction in a dynamical timescale, and become available again for cooling and star formation. The return rate decreases with halo mass. By following Guo et al. (2011), we have

$$\dot{M}_{\rm return} = -\gamma \left(\frac{V_{\rm vir}}{220 \text{ km s}^{-1}}\right)\left(\frac{M_{\rm out}}{t_{\rm dyn,h}}\right), \tag{17}$$

where $M_{\rm out}$ is the total mass of the outflow, and γ is a free parameter and is set to be 0.3 in our fiducial model. In the above scheme, supernova feedback is more efficient to heat the cold gas and suppress star formation in low-mass galaxies.

2.2.5 Black hole growth and AGN feedback

Following the first discovery of a BH in M32 (Tonry 1984), by the end of 2012, 87 more BHs had been discovered in the centers of galaxies (Kormendy & Ho 2013). More interestingly, there is a tight scaling relation between BH mass and stellar mass or velocity dispersion of the bulge of the host galaxy (e.g., Magorrian et al. 1998; Marconi & Hunt 2003; Gebhardt et al. 2000), indicating that the growths of a central BH and the associated bulge are regulated by each other. A simple way to build this scaling relation is mass averaging in galaxy mergers (Peng 2007; Jahnke & Macciò 2011). A scaling relation naturally arises between them, but only if they both grow mainly through galaxy mergers. Here we follow the scheme of Croton et al. (2006) to describe the growth of a BH, in which BH growth through both mergers and quiet accretion are considered.

In our model, when a galaxy forms, a BH seed is initialized in the center of the galaxy. The seed may be the remnant of first stars, with a mass of a few hundred solar masses. The initial mass of the seed is normally only a tiny fraction of its later mass because of its rapid growth, thus changing the initial seed mass almost has no effect on the evolution of the galaxy. In this model we set the seed mass to zero for simplicity.

BH growth in Croton et al. (2006) is divided into two different modes: "quasar" mode and "radio" mode. The quasar mode accounts for BH growth during mergers, which will be described later. Radio mode accounts for BH growth through accreting hot gas

$$\dot{M}_{\rm BH} = \kappa \left(\frac{M_{\rm hot}/M_{\rm vir}}{0.1}\right)\left(\frac{V_{\rm vir}}{200 \text{ km s}^{-1}}\right)^3 \left(\frac{M_{\rm BH}}{10^8\, h^{-1}\, M_\odot}\right) M_\odot \text{ yr}^{-1}, \tag{18}$$

where κ is a free parameter to describe the strength of accretion. When baryons fall into BHs, 10% of their rest mass energy is released to the CGM, heating surrounding gas and suppressing gas cooling

$$\dot{E}_{\rm radio} = 0.1\dot{M}_{\rm BH}c^2, \tag{19}$$

$$\dot{M}_{\rm cool,eff} = \dot{M}_{\rm cool} - 2\dot{E}_{\rm radio}/V_{\rm vir}^2. \tag{20}$$

$\dot{M}_{\rm cool,eff}$ is the effective cooling rate when considering suppression of AGN feedback.

As Equation (18) demonstrates, the strength of accretion depends strongly on the virial velocity of halos, $V_{\rm vir}$, and it is expected that the AGN feedback is more effective in more massive galaxies.

2.2.6 Bar formation

Not all stellar disks are stable. Toomre (1964) pointed out that only stellar disks with large radial velocity disper-

sion can suppress all axisymmetric instabilities, i.e., the equivalent of pressure resulting from motion must be large enough to overcome self-gravity and other instabilities. If the surface density of a galaxy's stellar disk is high and the self-gravity overwhelms the pressure, it could be unstable and may transform to a bar (Christodoulou et al. 1995; Mo et al. 1998). Efstathiou et al. (1982) used N-body simulations to explore disk instabilities, and derived a criterion to judge whether an exponential disk is stable. Here we utilize a modified form of De Lucia & Blaizot (2007): the cold gas disk is unstable if

$$M_{\rm disk,*} > \frac{3R_{\rm disk,*,d}V_{\rm max}^2}{G} \equiv M_{\rm disk,*,crit}. \quad (21)$$

When a transient bar forms, it will transfer stellar mass from the inner stellar disk to the bulge. After the transfer, the disk will be stable again, so we estimate the transferred mass as $M_{\rm bar} = M_{\rm disk,*} - M_{\rm disk,*,crit}$.

We follow Guo et al. (2011) to determine the radius of the transferred part, $R_{\rm bar}$

$$\begin{aligned} M_{\rm bar} =& \int_0^{R_{\rm bar}} \Sigma_{\rm disk,*,0} e^{-\frac{R}{R_{\rm disk,*,d}}} 2\pi R {\rm d}R \\ =& 2\pi\Sigma_{\rm disk,*,0} R_{\rm disk,*,d} \\ & \times \left[R_{\rm disk,*,d} - (R_{\rm bar} + R_{\rm disk,*,d})\, e^{-\frac{R_{\rm bar}}{R_{\rm disk,*,d}}} \right], \end{aligned} \quad (22)$$

where $\Sigma_{\rm disk,*,0}$ is the central surface density of the stellar disk, and $R_{\rm bar}$ is the estimated radius of the bar which can be solved numerically. The mass of the transferred part is added into the existing bulge and the size of the new bulge is calculated in the same way as if a merger occurred, which will be described later.

2.2.7 *Exchange of mass, metal and angular momentum*

When a galaxy evolves in isolation, all of the physical models should obey conservation laws, including mass and angular momentum. Figure 1 presents a cartoon plot illustrating the complex exchange of baryonic matter in our model. Below we summarize in detail the migration of mass, metal and angular momentum between different phases in our model.

To ensure that the total mass of a galaxy meets a certain fraction $f_{\rm b}$ of the host halo mass, we adjust the hot gas mass as

$$\begin{aligned} M_{\rm hot} =& f_{\rm b}M_{\rm vir} - M_{\rm disk,gas} - M_{\rm disk,*} \\ & - M_{\rm sph,gas} - M_{\rm sph,*} - M_{\rm out} - M_{\rm BH}, \end{aligned}$$

and

$$M_{\rm hot} \geq 0.$$

Therefore, the exchange of mass can be described by the following equations:

$$\begin{aligned} \delta M_{\rm hot} =& M_{\rm return} + M_{\rm reheat,disk} + M_{\rm reheat,sph} \\ & - M_{\rm eject} - M_{\rm cool,eff} - M_{\rm radio}, \end{aligned}$$

$$\delta M_{\rm disk,gas} = M_{\rm cool,eff} - M_{\rm SF,disk} - M_{\rm reheat,disk},$$

$$\delta M_{\rm disk,*} = M_{\rm SF,disk} - M_{\rm bar},$$

$$\delta M_{\rm sph,gas} = -M_{\rm SF,sph} - M_{\rm reheat,sph},$$

$$\delta M_{\rm sph,*} = M_{\rm SF,sph} + M_{\rm bar},$$

$$\delta M_{\rm out} = M_{\rm eject} - M_{\rm return},$$

$$\delta M_{\rm BH} = M_{\rm radio}.$$

The ISM of galaxies is enriched by metals released by stellar winds and supernova explosions. Metal enrichment was first included into semi-analytic models in White & Frenk (1991), in which metals are created in stellar evolution and then distributed into other components through mass transfer. The detailed metal exchange in our models is summarized as follows:

$$\begin{aligned} \delta M_{\rm z,hot} =& M_{\rm z,return} + M_{\rm z,reheat,disk} + M_{\rm z,reheat,sph} \\ & - M_{\rm z,eject} - M_{\rm z,cool,eff} - M_{\rm z,radio}, \end{aligned}$$

$$\begin{aligned} \delta M_{\rm z,disk,gas} =& M_{\rm z,cool,eff} - M_{\rm z,SF,disk} - M_{\rm z,reheat,disk} \\ & + y_{\rm z} M_{\rm SF,disk}, \end{aligned}$$

$$\delta M_{\rm z,disk,*} = M_{\rm z,SF,disk} - M_{\rm z,bar},$$

$$\delta M_{\rm z,sph,gas} = -M_{\rm z,SF,sph} - M_{\rm z,reheat,sph} + y_{\rm z} M_{\rm SF,sph},$$

$$\delta M_{\rm z,sph,*} = M_{\rm z,SF,sph} + M_{\rm z,bar},$$

$$\delta M_{\rm z,out} = M_{\rm z,eject} - M_{\rm z,return},$$

where $y_{\rm z} = 0.03$ is the so-called "yield," controlling the amount of metals created during stellar evolution. In our model, for simplicity, we assume the composition of metals to be solar value, and do not consider different elements independently. Figure 2 plots the metallicity in stars and gas as a function of stellar mass at $z = 0$ in our fiducial model. Our model agrees well with observational metallicity for stars. As for gaseous metallicity, our model is marginally in agreement with Blanc et al. (2019) for galaxies more massive than $10^{9.5}$ $M_\odot$ and is marginally in agreement with the lower limit of Lee et al.

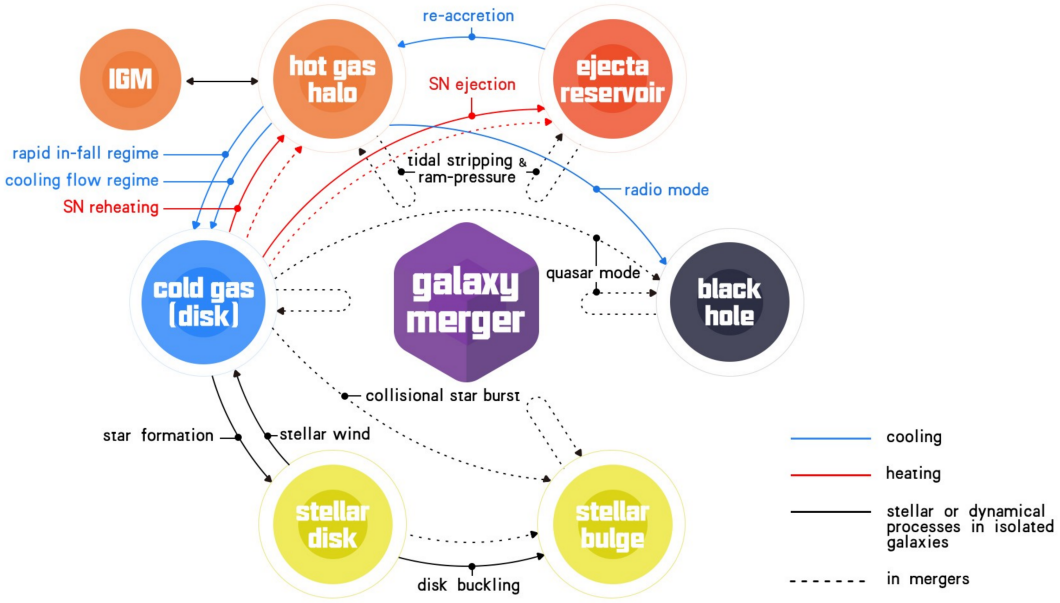

Fig. 1 A cartoon illustration of the baryonic exchange in GABE. *Blue* and *red lines* correspond to the cooling and heating processes in the evolution of a galaxy, respectively; *black lines* correspond to stellar or dynamical processes. *Solid lines* signify physical processes for galaxy evolution in isolation, described in Sect. 2.2; *dashed lines* indicate physical processes during galaxy interactions, described in Sect. 2.3.

(2006) for galaxies smaller than $10^{9.5}\ M_\odot$, but way below the observational result of Tremonti et al. (2004) for galaxies less massive than $10^{11}\ M_\odot$. This discrepancy between different observational results is caused by systematic uncertainties in the measurement of gaseous metallicity. Kewley & Ellison (2008) demonstrated that depending on the choice of metallicity calibration, the absolute metallicity normalization varies up to 0.7 dex. López-Sánchez et al. (2012) and Blanc et al. (2019) also demonstrated there is a discrepancy between different diagnostics, and which one is preferred has not been conclusively decided by the community. As illustrated in these equations, the amount of gaseous metallicity directly relates to galactic cooling, star formation, supernova feedback and AGN feedback. However, we choose not to use gaseous metallicity as a constraint or calibration for semi-analytic models before we have a clearer understanding of the systematic uncertainties in observations.

We follow Guo et al. (2011) and also consider the angular momentum transfer among different components. Generally it is assumed that the hot gas shares the same spin as its host dark matter halo, and the angular momentum of the cooled gas will be transferred into the galaxy when the stars begin to form. The full exchange of angular momentum can be summarized as the following:

$$\delta J_{\rm disk,gas} = J_{\rm cool,eff} - J_{\rm SF,disk} - J_{\rm reheat,disk},$$

$$\delta J_{\rm disk,*} = J_{\rm SF,disk} - J_{\rm bar},$$

$$\delta J_{\rm sph,gas} = -J_{\rm SF,sph} - J_{\rm reheat,sph},$$

$$\delta J_{\rm sph,*} = J_{\rm SF,sph} + J_{\rm bar},$$

$$\delta J_{\rm out} = J_{\rm eject} - J_{\rm return}.$$

The disk density profile is often assumed to be exponential, and its scale radius is then determined by the disk's angular moment. By assuming a flat circular velocity curve, the disk scale radius of a galaxy can be derived with

$$R_{\rm disk,gas,d} = \frac{J_{\rm disk,gas}}{2V_{\rm max}M_{\rm disk,gas}}, \tag{23}$$

$$R_{\rm disk,*,d} = \frac{J_{\rm disk,*}}{2V_{\rm max}M_{\rm disk,*}}. \tag{24}$$

2.3 Hierarchical Growth

So far, we focus on physical processes of galaxy formation in isolation. In the standard cold dark matter cosmology, structure formation is hierarchical, namely small systems form first, and then merge to form larger and larger systems. In this section, we will focus on physical processes relevant to mergers.

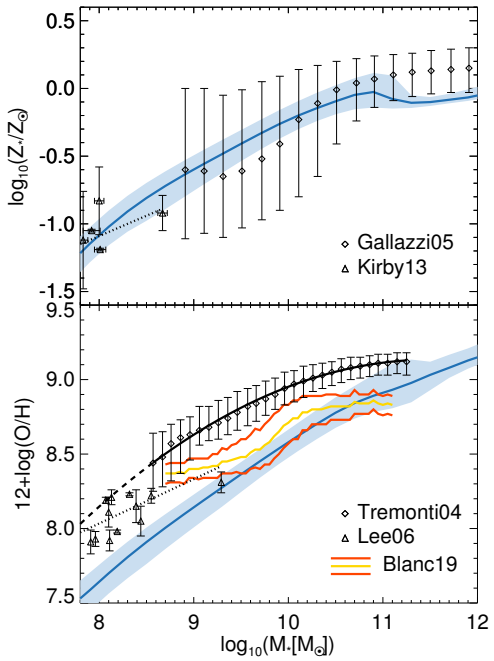

Fig. 2 Upper panel: the distribution of stellar metallicity in our model galaxies as a function of stellar mass at $z = 0$. The *blue solid line* shows the median values, and the *light blue area* indicates 16th and 84th percentiles. *Diamonds with error bars* signify the observational result of Gallazzi et al. (2005) from SDSS/DR2; and the *triangles with error bars* mark the observational result of Kirby et al. (2013), which is derived for local group dwarf galaxies. Lower panel: the distribution of gaseous metallicity in the star-forming galaxies (with specific star formation rate larger than $10^{-11}\,\mathrm{yr}^{-1}$) as a function of stellar mass at $z = 0$. *Diamonds with error bars* are the observational result of Tremonti et al. (2004) from SDSS. *Black solid line* is their fitting function and *dashed line* is the extrapolation to lower mass ranges. *Triangles with error bars* are the observational result of Lee et al. (2006) for nearby dwarf galaxies, and the *dotted line* is their fitting. The *yellow* and *red solid lines* are the mean value and 1σ scatter of the SDSS high mass sample in Blanc et al. (2019) respectively.

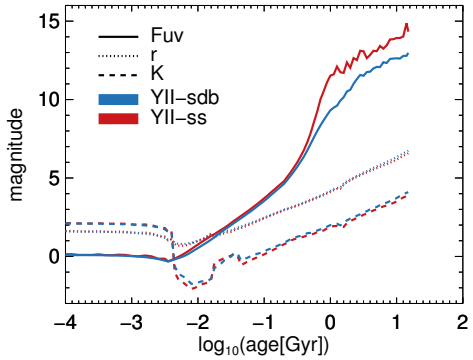

Fig. 3 Evolution of magnitudes in $F_{\rm UV}$, *r* and *K* band in *YII-sdb* and *YII-ss* assuming $1\,M_\odot$ stellar population with solar metallicity. Different lines and colors distinguish different bands and models as signified in the label.

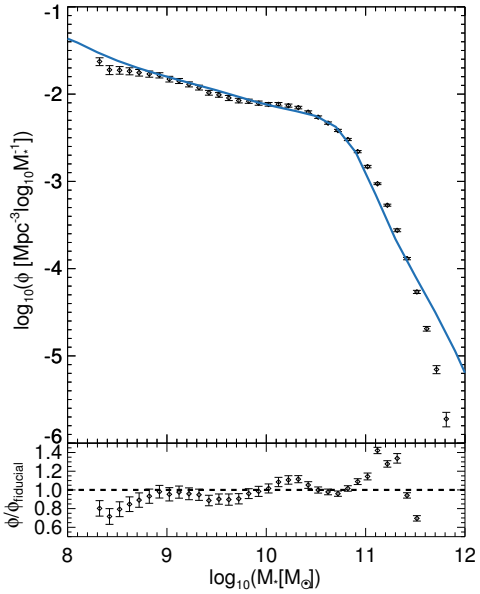

Fig. 4 Galaxy stellar mass functions at $z = 0$. The *blue line* shows the result of our fiducial model, and the *diamonds with error bars* signify observational result of Li & White (2009), using SDSS/DR7 data. The lower panel displays the ratios between our model and the observational results. The *black horizontal dashed line* indicates unity.

2.3.1 *Central and satellite galaxies*

When two halos approach closer and eventually merge into a single halo, the one with larger mass is called the primary halo, and the smaller one is called substructure of the primary halo and will eventually be tidally disrupted. Following Springel et al. (2001), the galaxy in the primary halo is called central galaxy ("type 0" galaxy), while the galaxy in the substructure is called a satellite galaxy. If a satellite galaxy has a host subhalo, then it is called "type 1" galaxy; and if not, it is called "type 2" galaxy. Central galaxies stay at the center of the primary halo, while satellite galaxies orbit around their main halo and suffer from tidal stripping, as well as ram-pressure stripping.

2.3.2 *Tidal and ram-pressure stripping of hot gas*

Tidal radius of a galaxy is a scale beyond which all dark matter and gas get tidally stripped, which can be estimated as

$$R_{\rm tidal} = R_{\rm vir,infall}\frac{M_{\rm vir}}{M_{\rm vir,infall}}, \qquad (25)$$

where $M_{\rm vir,infall}$ and $R_{\rm vir,infall}$ are the virial mass and radius of the satellite's host halo at the infall time[3], respectively.

[3] We define the moment at which the satellite last passes the virial radius of its host central halo as the "infall" time.

In addition to the tidal stripping, the hot gas component in satellites suffer ram-pressure stripping due to gas pressure from the primary halo. While ram-pressure stripping acts on both the hot and cold gas of satellites, in our model, for simplicity, we only implement this process to more extended hot gas component. The radius, $R_{\rm rp}$, of the hot gas of a satellite that is stripped by ram-pressure can be estimated by the balance of the pressure from the primary halo and the binding energy of the satellite

$$\rho_{\rm sat}\left(R_{\rm rp}\right) V_{\rm vir,sat}^2 = \rho_{\rm cen}\left(R_{\rm orbit}\right) V_{\rm orbit}^2, \qquad (26)$$

where $\rho_{\rm sat}\left(R_{\rm rp}\right)$ is gas density of the satellite at $R_{\rm rp}$, $V_{\rm vir,sat}$ is the virial velocity of the satellite, $\rho_{\rm cen}\left(R_{\rm orbit}\right)$ is the gas density of the central at the position of the satellite, and $V_{\rm orbit}$ is the relative velocity between the satellite and the central. In our model, we adopt the minimum of $[R_{\rm tidal}, R_{\rm rp}]$ to determine the radius beyond which hot gas from the satellite is stripped

$$R_{\rm strip} = \min\left(R_{\rm tidal}, R_{\rm rp}\right). \qquad (27)$$

2.3.3 Dynamical friction

When satellites orbit their central galaxies, they are dragged by the surrounding matter due to gravity, gradually lose energy and angular momentum and will eventually merge with the central galaxy. This process is called dynamical friction (Chandrasekhar 1943). Because our model is based on subhalo merging trees of N-body simulations, whether a subhalo survives in a merger may depend on employed numeric resolution. When a subhalo loses its identity in a simulation, namely below 20 particles, it is assumed that the stellar component of the subhalo (i.e., a type 2 galaxy) will still survive for a while because the stellar component is more compact than dark matter. Here we adopt the dynamical friction timescale fitting formula of Jiang et al. (2008) (hereafter Jiang08)

$$t_{\rm fric} = \frac{0.94\epsilon^{0.60}+0.60}{2C}\frac{M_{\rm cen}}{M_{\rm sat}}\frac{1}{\ln\left[1+\left(\frac{M_{\rm cen}}{M_{\rm sat}}\right)\right]}\frac{R_{\rm vir,cen}}{V_{\rm c}}, \qquad (28)$$

where ϵ is the circularity of the satellite orbit, $C = 0.43$ is a constant, $M_{\rm cen}$ is the primary dark matter halo mass, $M_{\rm sat}$ is the satellite mass, including dark matter halo and stars, and $V_{\rm c}$ is the circular velocity. $R_{\rm vir,cen}/V_{\rm c}$ represents free fall timescale in Jiang08, thus we use the virial velocity of central galaxy $V_{\rm vir,cen}$ to estimate $V_{\rm c}$. The circularity ϵ is calculated through eccentricity e (Wetzel 2011)

$$\epsilon = \sqrt{1-e^2}, \qquad (29)$$

$$e^2 = 1 + \frac{2E_{\rm orbit}J_{\rm orbit}}{\mu\left(GM_{\rm cen}M_{\rm sat}\right)^2}, \qquad (30)$$

where $E_{\rm orbit}$ and $J_{\rm orbit}$ are the total orbital energy and angular momentum of a satellite-central system, and $\mu = M_{\rm cen}M_{\rm sat}/(M_{\rm cen}+M_{\rm sat})$ is the reduced mass.

The dynamical friction timescale is calculated when the satellite first crosses the virial radius of its primary halo. After $t_{\rm fric}$, this satellite will merge into the central galaxy. This definition of $t_{\rm fric}$ is consistent with Jiang et al. (2008).

2.3.4 Remnants of mergers

Numerical simulations demonstrate that the remnants of mergers depend on the orbits and mass ratio of the two merging galaxies (Kannan et al. 2015). In our model, for simplicity, we follow White & Frenk (1991) to model the remnants of mergers based on the mass ratio of merging galaxies. If the mass ratio $f_{\rm merger} = M_{\rm sat}/M_{\rm cen}$ is greater than 0.3, then it is called a "major merger," otherwise it is called a "minor merger". For a major merger, all disk components of both satellite and central are destroyed to form spheroidal components, including cold gas and stars. For a minor merger, the smaller satellite will be destroyed completely in the end. Its gas component is added into the gaseous disk of the central, and the stellar component is added into the stellar bulge of the central. In both cases, the hot gas and outflow component will be simply added together correspondingly. The metals and angular momentum of each component will also be transferred along with mass.

2.3.5 Black hole growth in mergers

A very efficient mechanism for the growth of a BH is through mergers, especially major mergers. BHs accrete gas more easily (or effectively) in the violent dynamical environment during mergers. Following Kauffmann & Haehnelt (2000) and Croton et al. (2006), the growth of a central BH during mergers can be estimated as

$$\begin{aligned}\delta M_{\rm BH} = \quad & M_{\rm BH,sat} + f\left(\frac{M_{\rm sat}}{M_{\rm cen}}\right) \\ & \times\left[\frac{M_{\rm cold}}{1+\left(280\ {\rm km\ s^{-1}}/V_{\rm vir}\right)^2}\right], \end{aligned} \qquad (31)$$

where $M_{\rm BH,sat}$ is the BH mass of the satellite; $M_{\rm sat}$ and $M_{\rm cen}$ are the masses (cold gas and stars) of the satellite and the central galaxy, respectively; $M_{\rm cold}$ is the total mass of cold gas of two merging galaxies; and $V_{\rm vir}$ is the virial velocity of the primary halo. f is a free parameter controlling the growth rate of the central BH. In our fiducial model, we use $f = 0.03$ and can derive the tight relation between BH mass $M_{\rm BH}$ and bulge mass $M_{\rm sph,*}$ very well.

2.3.6 Star burst in mergers

Violent interactions during mergers can compress gas and trigger star bursts. We adopt the scheme "collisional starburst" of Somerville et al. (2001). In the model, the fraction of gas transferred into stars during a merger is

$$e_{\rm burst} = 0.56 \left(\frac{M_{\rm sat}}{M_{\rm cen}}\right)^{0.7}, \tag{32}$$

where $M_{\rm cen}$ and $M_{\rm sat}$ are the total mass (cold gas and stars) of the central and satellite galaxy, respectively. Along with the burst, supernova feedback releases a huge amount of energy. In a major merger, almost all the remaining cold gas is heated into the hot halo, strongly suppressing further star formation.

2.3.7 Bulge formation

Except for material from bar transfer, a galaxy merger is another important channel for bulge formation. We use the energy conservation scheme of Guo et al. (2011) to estimate the radius of the newly formed spheroidal remnant

$$\begin{aligned} C\frac{GM_{\rm new,bulge}^2}{R_{\rm new,bulge}} =& C\frac{GM_1^2}{R_1} + C\frac{GM_2^2}{R_2} \\ &+ \alpha_{\rm inter}\frac{GM_1M_2}{R_1+R_2}, \end{aligned} \tag{33}$$

where $C = 0.5$ is a structure parameter describing the binding energy of each system; $\alpha_{\rm inter} = 0.5$ is a parameter describing the interaction energy between systems; M_1, M_2 and $M_{\rm new,bulge}$ are the masses of progenitor systems and newly formed bulge, respectively; R_1, R_2 and $R_{\rm new,bulge}$ are the corresponding half-mass radii of progenitor systems and newly formed bulge, respectively. Equation (33) is also used to estimate the radius of the remnant after bar formation.

2.4 Luminosity of Galaxies

To compare our model with observations, we need to calculate the photometric properties of our model galaxies with an SPSM

$$\begin{aligned} L_\lambda =& 10^{-0.4(A_{\lambda,\rm ISM}+A_{\lambda,\rm BC})} \\ &\times \sum_{i=0}^{N_{\rm SP}} M_{\rm i} L_{\lambda,\rm i}(Z_{\rm i}, t-t_{\rm form,i}), \end{aligned} \tag{34}$$

where L_λ is the luminosity of a galaxy at wavelength λ; $L_{\lambda,\rm i}(Z,t)$ is the luminosity of unit solar mass stellar population with metallicity Z and age t at wavelength λ, which is provided by SPSMs; $N_{\rm SP}$ is the total number of stellar populations of the galaxy, $M_{\rm i}$, $Z_{\rm i}$ and $t_{\rm form,i}$ are the initial mass, metallicity and formation time of the ith stellar population, all of which are recorded during the running of GABE; $A_{\lambda,\rm ISM}$ and $A_{\lambda,\rm BC}$ are the reddening due to ISM and birth clouds, respectively, which are provided by dust extinction models.

2.4.1 Yunnan-II model: stellar population synthesis model with binary evolution

The SPSMs adopted in existing semi-analytic galaxy formation models are mostly based on single star stellar evolution models, e.g., BC03, BC07 with TP-AGBs and M05. However more than ∼50% of field stars in our Milky Way are in binary systems. Interactions between stars could produce some specific objects, such as blue stragglers (Pols & Marinus 1994) and subdwarf B stars (sdBs, Han et al. 2002), both of which would significantly alter the SED of the entire stellar population. In our model, we introduce binary interactions into galaxy formation and evolution by using the Yunnan-II SPSM (Zhang et al. 2004, 2005, 2010)[4].

Yunnan SPSMs are developed by the Group of Binary Population Synthesis, Yunnan Observatories, Chinese Academy of Sciences. The main differences among different versions of Yunnan models include the stellar evolution models, the evolutionary population synthesis construction method and the condition of binary interactions. The Yunnan-I model (Zhang et al. 2002) was constructed for stellar populations without binary interactions by applying the rapid single stellar evolution algorithms (Hurley et al. 2000) and used the "isochrone synthesis" technique. The Yunnan-II model was constructed for both stellar populations with and without binary interactions by implementing a Monte Carlo simulation and the rapid single and binary stellar evolution (BSE) algorithms (Hurley et al. 2000, 2002). In their latest version of the Yunnan-II model (Zhang et al. 2010), the evolutionary population synthesis models of Han et al. (2007) which included sdBs were also combined. The Yunnan-III model (Zhang et al. 2013) was constructed by employing single stars' evolutionary tracks obtained from the detailed MESA stellar evolution models (Paxton et al. 2011). Thus, the Yunnan-II model has a binary and a single version. The Yunnan-II model with full binary interactions is called *YII-sdb* hereafter and the one which has switched off binary interactions is called *YII-ss*. *YII-sdb* has modeled various binary interactions, including mass transfer, mass accretion, CE evolution, collisions, supernova kicks, tidal evolution, angular momentum loss, and so on.

Here we briefly describe the initial conditions and fiducial models adopted in the Yunnan-II model and BSE algorithm, while more details can be found in their pa-

[4] http://www1.ynao.ac.cn/~zhangfh/

pers. In building the Yunnan-II model, first 2.5×10^7 sets of initial conditions for binary evolution are created using the Monte Carlo method, including the masses of the primary and secondary star, orbital separation, eccentricity and metallicities of stars. The initial mass of the primary is generated by assuming a Chabrier (2003) IMF with cut-offs of $0.1\,M_\odot$ and $100\,M_\odot$, and a uniform initial secondary over primary mass ratio distribution is adopted. The initial orbital separation is taken to be constant in logarithm and initial eccentricity is distributed uniformly. In the fiducial model, 50% of field stars are assumed to be in binary systems. Actually, if the orbital separation is wide enough, there would be no interactions between component stars and they are effectively single. The stellar evolutionary tracks of generated binaries can be derived though the BSE algorithm. Most binary interactions are modeled through a prescription based approach (like galactic evolution models in semi-analytic models), and the properties of produced objects are comparable with many observations (e.g., cataclysmic variables, Algols, double-degenerates, etc., see section 4.3 of Hurley et al. 2002 for further details). Some model parameters have a major influence on the binary evolution, such as the efficiency of CE ejection $\alpha_{\rm CE}$ and Reimers wind mass-loss efficiency η. $\alpha_{\rm CE}$ describes the efficiency of the orbital energy dissipated by CE and decides whether the outcome of CE evolution is a close binary or a coalescence. The fiducial $\alpha_{\rm CE}$ in the Yunnan-II model is 3.0, increased from 1.0, to compensate the lack of internal energy in Hurley et al. (2002). Mass-loss is another crucial process in stellar evolution, and its rate often determines the final state of a binary system. The empirical formula of Kudritzki & Reimers (1978) is used and fiducial efficiency η is set to be 0.3 according to the observations of Galactic globular clusters (Iben & Renzini 1983). The influence of input model parameters on the integrated SED of stellar population was discussed in detail in section 4 of Zhang et al. (2005). They found that the differences between models with different parameters are less than those produced between models with and without binary interactions.

To explore the influence of binary evolution on the photometric properties of galaxies, we run our semi-analytic models with and without binary interactions. These two runs share the same semi-analytic models' parameters but adopt different SPSMs, and the comparison between these two runs will be demonstrated in Section 3.1. Figure 3 shows the magnitudes as a function of age in *YII-sdb* and *YII-ss* for a $1\,M_\odot$ stellar population with solar metallicity, and three photometric bands are shown: GALEX $F_{\rm UV}$ for UV band, SDSS *r* for optical band and 2MASS *K* for infrared band. In *r* and *K* bands, when considering binary interactions, the stellar population is fainter for stars older than $0.01\,{\rm Gyr}$. This effect is more obvious in *K* band than in *r* band. *YII-sdb* model is on average ~ 0.13 magnitude fainter than *YII-ss* in *K* band and ~ 0.07 magnitude fainter in *r* band for stars older than $0.01\,{\rm Gyr}$. While in UV band, the situation is reversed, and the stellar population considering binary interactions becomes brighter for stars older than $\sim 1\,{\rm Gyr}$ (~ 1.5 magnitude brighter on average). Because of this difference, binary stars are supposed to be responsible for the UV-excess in elliptical galaxies (Han et al. 2007). In summary, when considering binary interactions in an SPSM, luminosity is a bit fainter in the optical (~ 0.07 magnitude) and infrared band (~ 0.13 magnitude) but is significantly brighter in the far UV band (~ 1.5 magnitude).

2.4.2 Dust extinction

We adopt the dust extinction models of De Lucia & Blaizot (2007), including the extinction by diffuse ISM and birth clouds around young stars. The two reddening terms in Equation (34) are modeled as follows.

The reddening of a slab geometry ISM is given in Devriendt et al. (1999)

$$A_{\lambda,{\rm ISM}} = -2.5\log_{10} \times \left[\frac{1-\exp\left(-\sqrt{1-\omega_\lambda}\tau_\lambda^{\rm z}/\cos i\right)}{\sqrt{1-\omega_\lambda}\tau_\lambda^{\rm z}/\cos i}\right], \quad (35)$$

where ω_λ is the albedo of dust (Mathis et al. 1983); i is the inclination angle and can be estimated according to the direction of spin of a gaseous disk assuming the line-of-sight is along the third axis of N-body simulation; $\tau_\lambda^{\rm z}$ is the mean face-on optical depth of the average disk at wavelength λ

$$\tau_\lambda^{\rm z} = \left(\frac{A_\lambda}{A_{\rm V}}\right)_{z_\odot}\left(\frac{Z_{\rm g}}{Z_\odot}\right)^s \times \left(\frac{\langle N_{\rm H}\rangle}{2.1\times10^{21}{\rm cm}^{-2}}\right)(1+z)^{-0.4}, \quad (36)$$

$$\langle N_{\rm H}\rangle = \frac{M_{\rm disk,gas}}{1.4 m_{\rm p}\pi\left(aR_{\rm half,disk,gas}\right)}{\rm cm}^{-2}. \quad (37)$$

The first part of Equation (36) describes the extinction at the given wavelength relative to the extinction at $5500\,$Å(Mathis et al. 1983); the second part represents the dependence of extinction on gas metallicity ($s = 1.35$ for $\lambda < 2000\,$Åand $s = 1.6$ for $\lambda > 2000\,$Å, Guiderdoni & Rocca-Volmerange 1987); the last part corresponds to the dependence on redshift (Guo & White 2009). $\langle N_{\rm H}\rangle$ is the mean H column density and $a = 1.68$ in Equation (37).

The reddening for the birth clouds around young stars is given in Charlot & Fall (2000) and De Lucia & Blaizot (2007)

$$A_{\lambda,{\rm BC}} = -2.5\log_{10} e^{-\tau_{\lambda,{\rm BC}}}, \quad (38)$$

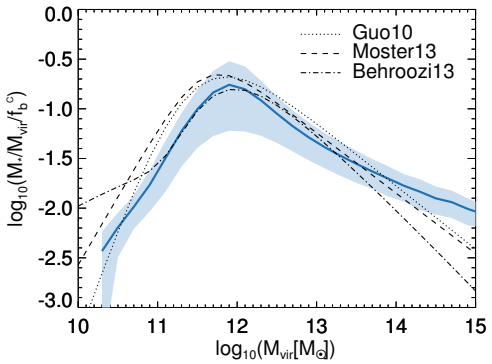

Fig. 5 Relation between central galaxy stellar mass and host halo mass. The *blue solid line* shows the mean value in each mass bin for central galaxies in our fiducial model. The *light blue shadow* indicates 16th and 84th percentiles. *Black lines* signify results from subhalo abundance matching models (*dotted*, Guo et al. 2010; *dashed*, Moster et al. 2013; *dot-dashed*, Behroozi et al. 2013).

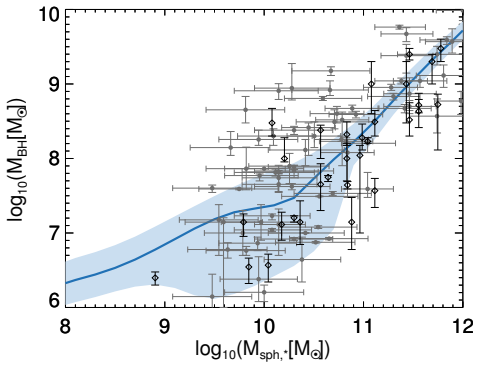

Fig. 6 The relation between BH and stellar bulge masses at $z = 0$. The *blue line* shows median values of our fiducial model, and the *light blue shadow* indicates 16th and 84th percentiles. The *black diamonds with error bars* are the observational result of Häring & Rix (2004). The *gray filled cycles with error bars* signify the observational result of Scott et al. (2013).

$$\tau_{\lambda,\mathrm{BC}} = \tau_\lambda^z \left(\frac{1}{\mu} - 1\right) \left(\frac{\lambda}{5500\text{Å}}\right)^{-0.7}, \qquad (39)$$

where μ is a random number drawn from a Gaussian distribution with mean 0.3 and standard deviation 0.2, truncated at 0.1 and 1 (Kong et al. 2004).

2.5 Model Calibration by Observation

In our whole set of physical models, a few parameters are set free and need to be calibrated according to observational data. Similar to Croton et al. (2006) and Guo et al. (2011), we have nine free parameters in our models which are summarized in Table 1. We adjust these parameters within the plausible ranges provided by Croton et al. (2006) to fit the stellar mass function at $z = 0$, and simultaneously to obtain a reasonable $M_{\mathrm{sph},*} - M_{\mathrm{BH}}$ scaling relation and stellar disk sizes. The fiducial values of these parameters are listed in Table 1. By adopting these fiducial values and *YII-sdb*, we are able to build our fiducial model.

Figure 4 presents galaxy stellar mass function at $z = 0$ in our fiducial model. We can see that the predicted stellar mass function agrees very well with the observational result of Li & White (2009). Only at the most massive end, with $M > 10^{11.5}\,M_\odot$, is the number density slightly higher than observation. To have a better understanding of the inconsistency, we plot the stellar mass of central galaxies against their host halo mass in Figure 5. Compared to subhalo abundance matching results of Guo et al. (2010), Moster et al. (2013) and Behroozi et al. (2013), our model predicts too massive galaxies in halos $> 10^{13.5}\,M_\odot$. Tuning parameters in the reasonable range can only improve the situation. Note, such an excess at the most massive end also exists in other semi-analytic models, such as Croton et al. (2006) and Guo et al. (2011). However, more recent semi-analytic models seem to be able to overcome this problem with improved AGN feedback models (Croton et al. 2016 and Henriques et al. 2015). We will explore this aspect in our future work.

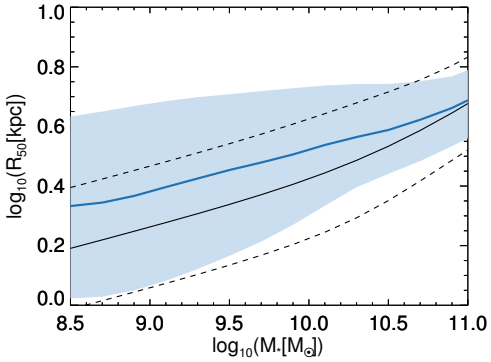

Fig. 7 The distribution of half mass radius of stellar disks for late type galaxies ($M_{\mathrm{disk},*}/(M_{\mathrm{disk},*} + M_{\mathrm{sph},*}) > 0.8$) as a function of stellar mass in our fiducial model. The *blue solid line* represents the median values of our model galaxies, and the *light blue shadow* indicates 16th and 84th percentiles. The *black solid line* signifies the fitting formula of the observational results from Shen et al. (2003), and the *dashed lines* show 1σ scatters.

Figure 6 depicts the BH to stellar bulge mass scaling relation in our fiducial model. Our results agree well with the observations but display slightly smaller scatter than observations. This is acceptable given the fact that the systematic errors of the observation are large.

Figure 7 is the distribution of the half mass radius of stellar disks for late type galaxies in our fiducial model. Our model's prediction is shown as the blue solid curve, while the observational data from Shen et al. (2003) are presented as the black solid and dashed lines. Again, the radius of stellar disks in our model agrees well with the observational data in most of the mass range. There is a slight disagreement at the small mass end, which is accept-

Table 1 Free Parameters in GABE and Their Fiducial Values

Parameter	Description	Fiducial Value
α	Star formation efficiency, Equation (9)	0.02
ϵ	Amplitude of supernova reheating efficiency, Equation (13)	6.5
β_1	Slope of supernova reheating efficiency, Equation (13)	3.5
η	Amplitude of supernova ejection efficiency, Equation (16)	0.32
β_2	Slope of supernova ejection efficiency, Equation (16)	3.5
$V_{\rm max,c}$	Characteristic $V_{\rm max}$ in supernova efficiency, Equation (13) and Equation (16)	90 km s^{-1}
γ	Outflow return efficiency, Equation (17)	0.3
f	BH growth efficiency in mergers, Equation (31)	0.03
κ	Quiescent BH accretion rate, Equation (18)	8.64×10^{-4}

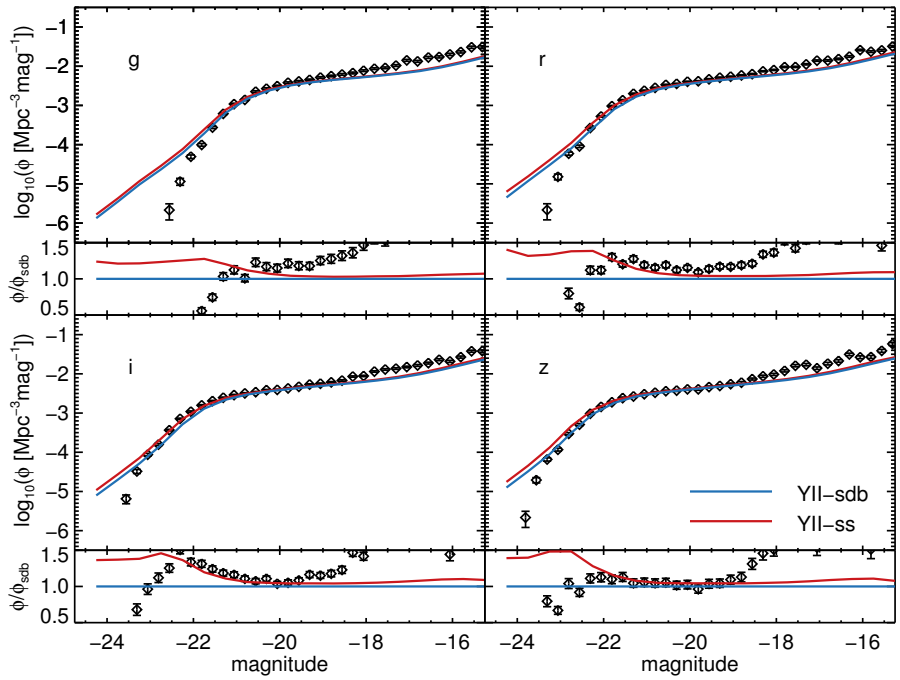

Fig. 8 The luminosity function of galaxies at $z = 0$ in the SDSS *g*, *r*, *i* and *z* bands. The *red* and *blue lines* signify results with Yunnan-II SPSMs *YII-sdb* and *YII-ss*) respectively. The *diamonds with error bars* indicate the observational result from SDSS/DR2 (Blanton et al. 2005). In each panel, the ratio between two Yunnan-II models and the ratio between SDSS and *YII-sdb* results are displayed at the bottom.

able given the fact that the uncertainty in measurement of galaxies size is also large at this mass scale.

3 RESULTS

3.1 The Influence of Binary Evolution

In the following, we examine the influence of adopting Yunnan-II SPSM on the galaxy luminosity function at different bands and galaxy colors.

3.1.1 Luminosity functions

In Figure 8, we present the luminosity function of galaxies at $z = 0$ in the SDSS *g*, *r*, *i* and *z* bands. The results with *YII-sdb* and *YII-ss* are shown as blue and red lines, respectively, while the observed data from SDSS are marked as diamonds with error bars. The ratio of the observed data or the *YII-ss* over *YII-sdb* model is displayed in the bottom panels. We see that the luminosity functions in both models agree well with the observational result over most magnitude scales. At the brightest end, the model prediction is higher than the observational data. Cosmic variance could be partly responsible for that. At the faint end with $M > -18$, our model prediction is lower than the observations because the resolution is not enough for these faint galaxies in the Millennium simulation. Furthermore, in all bands, the difference between two Yunnan-II models is very tiny at the faint galaxy end (less than 10%), but the difference can be $20\% \sim 50\%$ for galaxies above the character luminosity (the "knee" of luminosity function). Binary interactions have a similar behavior for galaxies' luminosity and simple stellar population (as shown in Fig. 3). They make galaxies fainter in all optical bands, hence they lower the luminosity function. In addition, this

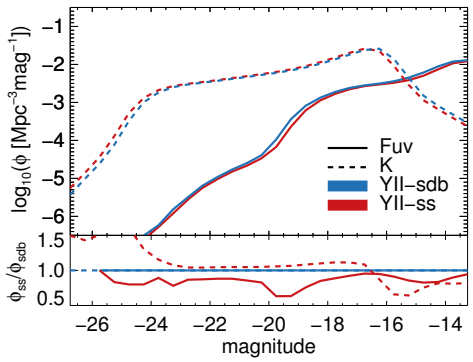

Fig. 9 In the top panel, the luminosity function of galaxies in our fiducial model at $z = 0$ in the GALEX $F_{\rm UV}$ band and 2MASS *K* band are presented as *solid* and *dashed lines* respectively. The two Yunnan-II SPSMs models, *YII-sdb* and *YII-ss* are indicated as *blue* and *red*, respectively. The ratio of the results from two SPSMs models is presented in the bottom panel.

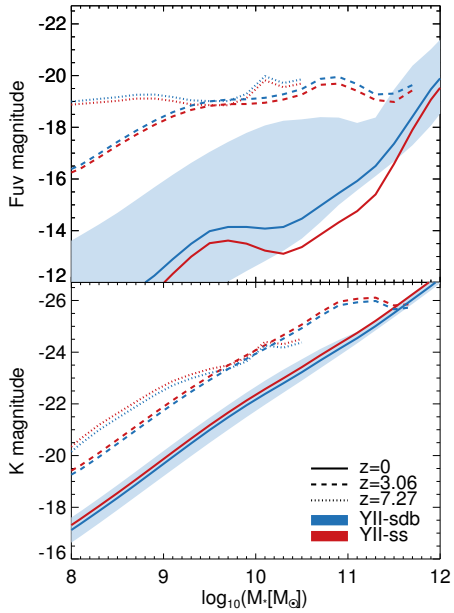

Fig. 10 The luminosity of our model galaxies in $F_{\rm UV}$ and *K* bands is presented as a function of the stellar mass in top and bottom panels respectively. The median values in each mass bin from two Yunnan-II models, *YII-sdb* and *YII-ss*), are shown as *blue* and *red* respectively. The results from different redshifts $z = 0, 3.06, 7.27$ are signified with *solid*, *dashed* and *dotted curves* respectively. The *blue shaded regions* indicate 16th and 84th percentiles for the *YII-sdb* model at $z = 0$.

effect becomes a bit more obvious at longer wavelengths. After considering binary interactions, the average shifts of luminosity functions along the x-axis are 0.10, 0.14, 0.15 and 0.16 magnitude for *g*, *r*, *i* and *z* bands respectively.

As depicted in Figure 3, the evolution of a simple stellar population with two Yunnan-II models only differs from each other by $\sim$ 0.07 magnitude in optical bands, which agrees with what we see in Figure 8. In addition, it is expected that the difference would be larger in *K* band and $F_{\rm UV}$ band, especially when the population gets older. Therefore, we checked that in Figure 9, in which we presented the luminosity function of galaxies from two SPSMs models in GALEX $F_{\rm UV}$ band and 2MASS *K* band with solid and dashed lines, respectively. The ratio of the two models is also presented in the bottom panel. In $F_{\rm UV}$ band, the results of the binary evolution model *YII-sdb* are always higher than those of *YII-ss*, which indicate galaxies get brighter if the binary evolution is included. The situation is reversed in *K* band. Galaxies with binary evolution become fainter, as what we see in the optical bands, but more obvious. After considering binary interactions, the average shifts of luminosity functions along x-axis are -0.20 and 0.18 magnitude for $F_{\rm UV}$ and *K* bands respectively.

To further understand the difference in the luminosity function between the two Yunnan-II models described above, we explore the relation between galaxies' magnitude and their stellar mass in the $F_{\rm UV}$ and *K* bands for two Yunnan-II models in the upper and lower panels of Figure 10 respectively. It is notable that, for a given stellar mass in a galaxy, the $F_{\rm UV}$ luminosity is always brighter when the binary evolution is considered. In particular, for galaxies with a stellar mass of $\sim 10^{10.5}\,M_\odot$ at $z = 0$, the difference is significant and reaches $\sim$ 1.5 magnitude. This overall excess originates from binary interactions, which will bring about an excess in the $F_{\rm UV}$ band in old stellar populations. We have checked to make sure that most of this excess is contributed by early type galaxies, and the $F_{\rm UV}$ luminosity of late type galaxies is less influenced by binary interactions. The results at redshift $z = 0, 3.06, 7.27$ are also shown by different types of lines. It is obvious that the difference is smaller at higher redshift. This happens because the difference between two SPSMs becomes larger when the populations in galaxies get older. The results are reversed for *K* band in the bottom panel. The *K* magnitude in *YII-ss* is always brighter than that with binaries considered for all mass scales and redshifts. The suppression of the formation of red giants by the interactions in binaries is supposed to be responsible for this.

In summary, the inclusion of binary evolution will suppress the galaxies' luminosity in optical and infrared bands (SDSS bands and 2MASS *K* band) slightly, but will increase the luminosity at the UV band significantly. The displacements of luminosity function along magnitude are $0.10 \sim 0.16$, 0.18 and -0.20 in SDSS bands, *K* band and $F_{\rm UV}$ band respectively. However, given the big scatter in the models (blue shaded region in Fig. 10) and the huge uncertainties in the observations, the difference between the two SPSMs models is still not distinguishable in the current observational data.

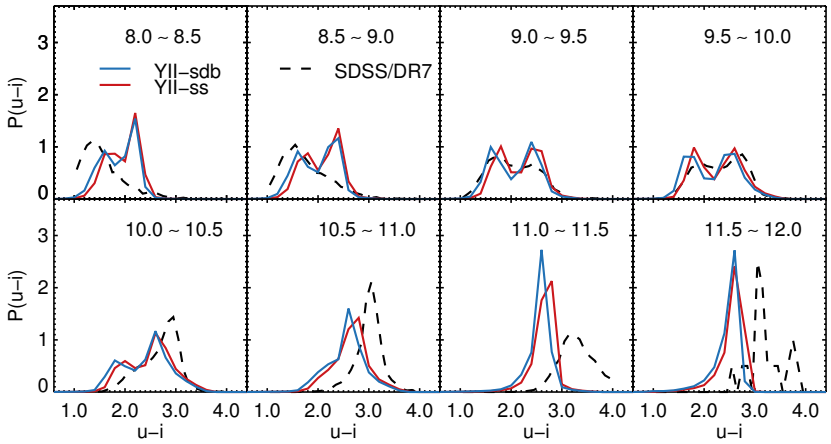

Fig. 11 (u - i) color distribution of our model galaxies in different stellar mass ranges. The results of Yunnan-II models, *YII-sdb* and *YII-ss*, are presented as *red* and *blue lines respectively*.

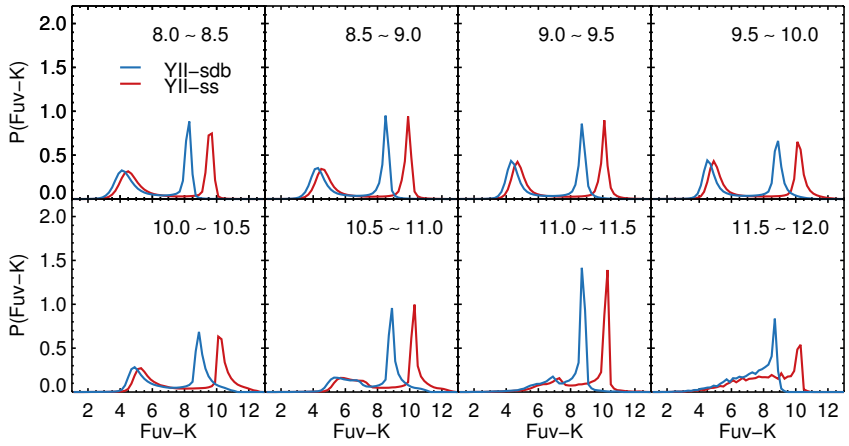

Fig. 12 ($F_{\rm UV}$ - K) color distribution of our model galaxies in different stellar mass ranges. The results of Yunnan-II models, *YII-sdb* and *YII-ss*, are presented as *red* and *blue lines respectively*.

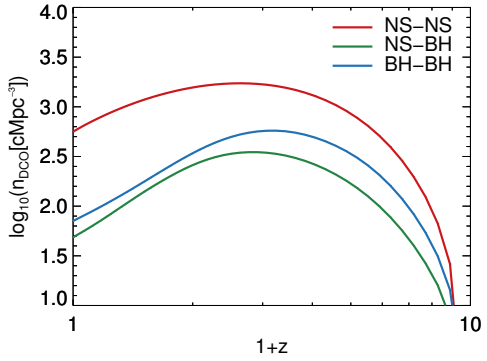

Fig. 13 The predicted cosmic number per cubic comoving volume of DCOs (including NS-NS, NS-BH and BH-BH) as a function of redshift in our fiducial model. Different colors show results for different DCOs as indicated in the label.

3.1.2 Color distribution

Furthermore, we checked the color index u - i distribution of our model galaxies in different stellar mass bins in Figure 11. The results from two SPSMs models, *YII-sdb* and *YII-ss*, are presented with blue and red solid curves respectively; and the observational data from SDSS are shown as black dashed curves. Generally, our fiducial model with *YII-sdb* can recover bimodality of the color distribution in SDSS data in the stellar mass range $[10^{9.0}, 10^{10.5}]\,M_{\odot}$. But at the massive end, our model predictions are bluer than observations, and at the faint end, our model galaxies are redder than the observed result. As Henriques et al. (2015) pointed out, to get the correct prediction on the color distribution, some physical models need to be updated or even some new physics may be needed. Moreover, the galaxies in *YII-sdb* are ~ 0.1 bluer.

Because the influences of binary evolution on galaxies' flux in $F_{\rm UV}$ and K band are bigger, it is supposed that the color index between these two bands will change significantly when the binary evolution is included. In Figure 12, the color index $F_{\rm UV}-K$ is presented for both Yunnan-II models. The bimodality feature is apparent.

With binary evolution, the blue peak is shifted towards the blue end by ~ 0.4, and the red peak is shifted towards the blue end by ~ 1.6, which is three times larger than the blue peak. The galaxies in *YII-sdb* are brighter in $F_{\rm UV}$ band because of the existence of hot stars, so they have smaller $F_{\rm UV}-K$ and are shifted to the left in every panel compared to the model prediction of *YII-ss*. The red peak corresponds to old galaxies which are influenced substantially by binary evolution in $F_{\rm UV}$ band (as shown in Fig. 3), thus shift of the red peak is much larger than that of the blue peak. If the observational $F_{\rm UV}$ magnitudes could be constrained better in the future, it is very promising that we will be able to tell the difference between these two model predictions with the observations.

3.2 Remnants of Binary Evolution

The remnants of the evolution of binary stars (e.g., NS-NS, NS-BH, BH-BH) are thought to be associated with many high energy events, such as type Ia supernovae, short gamma-ray bursts, kilnovae and gravitational wave events. In our model, using Yunnan-II binary SPSM, we are able to study these remnants in a cosmological context. For example, in Figure 13 we show the cosmic number density of DCOs, i.e., NS-NS, NS-BH and BH-BH as a function of cosmic time. With the number density and merger rate of these DCOs, we could study some high energy events associated with mergers of them, such as gravitational wave signals, kilonovae, short gamma-ray bursts, etc. We will present these results in our forthcoming papers.

4 CONCLUSIONS

In this work, we develop a new semi-analytic galaxy formation model GABE. This model is based on merger trees provided by cosmological N-body simulations. It incorporates many physical recipes from existing successful models and also includes some new ingredients. For example, it adopts Yunnan-II SPSM which carefully considers binary evolution, and a cooling table, which properly takes into account UV heating.

When calibrating our model to the observed stellar mass function, our model reproduces a large body of observations. We explore the influence of the Yunnan SPSM model with binary evolution on the galaxy luminosity function and color. Our finding is that, with binary SPSM, the influence on luminosity is quite small over different SDSS bands, and is more substantial in the infrared band and the UV band. The shifts of luminosity function along magnitude after considering binary evolution are $0.10 \sim 0.16$, 0.18 and -0.20 magnitude in SDSS bands, *K* band and $F_{\rm UV}$ band respectively. Galaxies appear to be bluer with binary evolution, especially when $F_{\rm UV}$ band is under consideration. The shift of *u* - *i* color index is about -0.1. The shift of the blue peak of $F_{\rm UV}-K$ color index is about -0.4, and the shift of the red peak is about -1.6, three times larger than the blue peak.

This is the first paper in our series of works. We have used GABE to simulate the gravitational wave signals of supermassive BHs in Wang et al. (2019). The new feature of our model allows us to predict the population of DCOs (e.g., NS-NS, NS-BH and BH-BH) which are expected to be associated with some high energy events in a cosmological context. For example, the short gamma-ray bursts are expected to be products of NS-NS or NS-BH mergers, and gravitational wave events are supposed to be generated during mergers of two compact objects in binary systems. In addition, we will be able to explore the relationship between these high energy events and their host galaxies. We will present these studies in our future works.

Acknowledgements We acknowledge Zhanwen Han for reading our draft and providing some very useful comments and suggestions. We also would like to thank the anonymous referee for an insightful report which led to improvements in the presentation and content of our paper. We acknowledge support from the National Key Program for Science and Technology Research and Development (2015CB857005, 2017YFB0203300) and the National Natural Science Foundation of China (Grant Nos. 11390372, 11425312, 11503032, 11573031, 11851301, 11873051, 11573062, 11521303, 11390734, 11573033, 11622325 and 11573030). In addition, FZ acknowledges support from the YIPACAS Foundation (Grant No. 2012048) and the Yunnan Foundation (2011CI053). QG is supported by the Newton Advanced Fellowship. JP acknowledges support from the National Basic Research Program of China (program 973; 2015CB857001).

References

Behroozi, P. S., Wechsler, R. H., & Conroy, C. 2013, ApJ, 770, 57

Benson, A. 2011, Galacticus: A Semi-Analytic Model of Galaxy Formation, Astrophysics Source Code Library, ascl:1108.004

Blanc, G. A., Lu, Y., Benson, A., et al. 2019, arXiv:1904.02721

Blanton, M. R., Lupton, R. H., Schlegel, D. J., et al. 2005, ApJ, 631, 208

Bruzual, G. 2007, ASP Conf. Ser., 374, From Stars to Galaxies: Building the Pieces to Build Up the Universe, eds. A. Vallenari, R. Tantalo, L. Portinari, & A. Moretti, 303

Bruzual, G., & Charlot, S. 2003, MNRAS, 344, 1000

Chabrier, G. 2003, PASP, 115, 763

Chandrasekhar, S. 1943, ApJ, 97, 255

Charlot, S., & Fall, S. M. 2000, ApJ, 539, 718

Christodoulou, D. M., Shlosman, I., & Tohline, J. E. 1995, ApJ, 443, 551
Colless, M., & et al. 2001, MNRAS, 328, 1039
Croton, D. J., Springel, V., White, S. D. M., et al. 2006, MNRAS, 365, 11
Croton, D. J., Stevens, A. R. H., Tonini, C., et al. 2016, ApJS, 222, 22
De Lucia, G., & Blaizot, J. 2007, MNRAS, 375, 2
De Lucia, G., Tornatore, L., Frenk, C. S., et al. 2014, MNRAS, 445, 970
Devriendt, J. E. G., Guiderdoni, B., & Sadat, R. 1999, A&A, 350, 381
Duquennoy, A., & Mayor, M. 1991, A&A, 248, 485
Efstathiou, G. 1992, MNRAS, 256, 43P
Efstathiou, G., Lake, G., & Negroponte, J. 1982, MNRAS, 199, 1069
Gallazzi, A., Charlot, S., Brinchmann, J., et al. 2005, MNRAS, 362, 41
Gebhardt, K., Bender, R., Bower, G., et al. 2000, ApJ, 539, L13
Gnedin, N. Y. 2000, ApJ, 542, 535
Guiderdoni, B., & Rocca-Volmerange, B. 1987, A&A, 186, 1
Guo, Q., & White, S. D. M. 2009, MNRAS, 396, 39
Guo, Q., White, S., Li, C., et al. 2010, MNRAS, 404, 1111
Guo, Q., White, S., Boylan-Kolchin, M., et al. 2011, MNRAS, 413, 101
Han, Z., Podsiadlowski, P., & Lynas-Gray, A. E. 2007, MNRAS, 380, 1098
Han, Z., Podsiadlowski, P., Maxted, P. F. L., et al. 2002, MNRAS, 336, 449
Häring, N., & Rix, H.-W. 2004, ApJ, 604, L89
Henriques, B. M. B., White, S. D. M., Thomas, P. A., et al. 2015, MNRAS, 451, 2663
Hurley, J. R., Pols, O. R., & Tout, C. A. 2000, MNRAS, 315, 543
Hurley, J. R., Tout, C. A., & Pols, O. R. 2002, MNRAS, 329, 897
Iben, Jr., I., & Renzini, A. 1983, ARA&A, 21, 271
Iben, Jr., I., & Tutukov, A. V. 1984, ApJS, 54, 335
Jahnke, K., & Macciò, A. V. 2011, ApJ, 734, 92
Jiang, C. Y., Jing, Y. P., Faltenbacher, A., et al. 2008, ApJ, 675, 1095
Jiang, L., Helly, J. C., Cole, S., et al. 2014, MNRAS, 440, 2115
Kannan, R., Macciò, A. V., Fontanot, F., et al. 2015, MNRAS, 452, 4347
Kauffmann, G. 1996, MNRAS, 281, 475
Kauffmann, G., Colberg, J. M., Diaferio, A., et al. 1999, MNRAS, 303, 188
Kauffmann, G., & Haehnelt, M. 2000, MNRAS, 311, 576
Kewley, L. J., & Ellison, S. L. 2008, ApJ, 681, 1183
Kirby, E. N., Cohen, J. G., Guhathakurta, P., et al. 2013, ApJ, 779, 102
Kong, X., Charlot, S., Brinchmann, J., & Fall, S. M. 2004, MNRAS, 349, 769
Kormendy, J., & Ho, L. C. 2013, ARA&A, 51, 511
Kudritzki, R. P., & Reimers, D. 1978, A&A, 70, 227
Lee, H., Skillman, E. D., Cannon, J. M., et al. 2006, ApJ, 647, 970
Li, C., & White, S. D. M. 2009, MNRAS, 398, 2177
López-Sánchez, Á. R., Dopita, M. A., Kewley, L. J., et al. 2012, MNRAS, 426, 2630
Magorrian, J., Tremaine, S., Richstone, D., et al. 1998, AJ, 115, 2285
Mapelli, M., Giacobbo, N., Ripamonti, E., & Spera, M. 2017, MNRAS, 472, 2422
Maraston, C. 2005, MNRAS, 362, 799
Marconi, A., & Hunt, L. K. 2003, ApJ, 589, L21
Mathis, J. S., Mezger, P. G., & Panagia, N. 1983, A&A, 128, 212
Mo, H. J., Mao, S., & White, S. D. M. 1998, MNRAS, 295, 319
Moster, B. P., Naab, T., & White, S. D. M. 2013, MNRAS, 428, 3121
Narayan, R., Paczynski, B., & Piran, T. 1992, ApJ, 395, L83
Nelson, D., Springel, V., Pillepich, A., et al. 2018, arXiv:1812.05609
Okamoto, T., Gao, L., & Theuns, T. 2008, MNRAS, 390, 920
Paxton, B., Bildsten, L., Dotter, A., et al. 2011, ApJS, 192, 3
Peng, C. Y. 2007, ApJ, 671, 1098
Pols, O. R., & Marinus, M. 1994, A&A, 288, 745
Sana, H., de Mink, S. E., de Koter, A., et al. 2012, Science, 337, 444
Schaye, J., Crain, R. A., Bower, R. G., et al. 2015, MNRAS, 446, 521
Scott, N., Graham, A. W., & Schombert, J. 2013, ApJ, 768, 76
Shen, S., Mo, H. J., White, S. D. M., et al. 2003, MNRAS, 343, 978
Somerville, R. S., Primack, J. R., & Faber, S. M. 2001, MNRAS, 320, 504
Spergel, D. N., Verde, L., Peiris, H. V., et al. 2003, ApJS, 148, 175
Springel, V., White, S. D. M., Tormen, G., & Kauffmann, G. 2001, MNRAS, 328, 726
Springel, V., White, S. D. M., Jenkins, A., et al. 2005, Nature, 435, 629
Sutherland, R. S., & Dopita, M. A. 1993, ApJS, 88, 253
Tonry, J. L. 1984, ApJ, 283, 27
Toomre, A. 1964, ApJ, 139, 1217
Totani, T. 2013, PASJ, 65, L12
Tremonti, C. A., Heckman, T. M., Kauffmann, G., et al. 2004, ApJ, 613, 898
Wang, H.-T., Jiang, Z., Sesana, A., et al. 2019, arXiv:1902.04423
Wang, J.-S., Yang, Y.-P., Wu, X.-F., et al. 2016, ApJ, 822, L7
Wetzel, A. R. 2011, MNRAS, 412, 49
Whelan, J., & Iben, Jr., I. 1973, ApJ, 186, 1007
White, S. D. M., & Frenk, C. S. 1991, ApJ, 379, 52
Wiersma, R. P. C., Schaye, J., & Smith, B. D. 2009, MNRAS, 393, 99
Zhang, F., Han, Z., Li, L., et al. 2010, Ap&SS, 329, 249
Zhang, F., Han, Z., Li, L., et al. 2002, MNRAS, 334, 883
Zhang, F., Han, Z., Li, L., et al. 2004, A&A, 415, 117
Zhang, F., Han, Z., Li, L., et al. 2005, MNRAS, 357, 1088
Zhang, F., Li, L., Han, Z., et al. 2013, MNRAS, 428, 3390